

Simplified Analysis of Low-Thrust Orbital Maneuvers

15 August 2000

Prepared by

J. E. POLLARD
Propulsion Science & Experimental Mechanics Department
Space Materials Laboratory

Prepared for

SPACE AND MISSILE SYSTEMS CENTER
AIR FORCE MATERIEL COMMAND
2430 E. El Segundo Boulevard
Los Angeles Air Force Base, CA 90245

Engineering and Technology Group

APPROVED FOR PUBLIC RELEASE;
DISTRIBUTION UNLIMITED


THIS QUALITY INSPECTED 4

20001116 052

This report was submitted by The Aerospace Corporation, El Segundo, CA 90245-4691, under Contract No. F04701-93-C-0094 with the Space and Missile Systems Center, 2430 E. El Segundo Blvd., Los Angeles Air Force Base, CA 90245. It was reviewed and approved for The Aerospace Corporation by P. D. Fleischauer, Principal Director, Space Materials Laboratory. M. Zambrana was the project officer for the Mission-Oriented Investigation and Experimentation (MOIE) program.

This report has been reviewed by the Public Affairs Office (PAS) and is releasable to the National Technical Information Service (NTIS). At NTIS, it will be available to the general public, including foreign nationals.

This technical report has been reviewed and is approved for publication. Publication of this report does not constitute Air Force approval of the report's findings or conclusions. It is published only for the exchange and stimulation of ideas.



M. Zambrana
Project Officer

REPORT DOCUMENTATION PAGE

Form Approved
OMB No. 0704-0188

Public reporting burden for this collection of information is estimated to average 1 hour per response, including the time for reviewing instructions, searching existing data sources, gathering and maintaining the data needed, and completing and reviewing the collection of information. Send comments regarding this burden estimate or any other aspect of this collection of information, including suggestions for reducing this burden to Washington Headquarters Services, Directorate for Information Operations and Reports, 1215 Jefferson Davis Highway, Suite 1204, Arlington, VA 22202-4302, and to the Office of Management and Budget, Paperwork Reduction Project (0704-0188), Washington, DC 20503.

1. AGENCY USE ONLY (Leave blank)		2. REPORT DATE 15 August 2000		3. REPORT TYPE AND DATES COVERED	
4. TITLE AND SUBTITLE Simplified Analysis of Low-Thrust Orbital Maneuvers				5. FUNDING NUMBERS F04701-93-C-0094	
6. AUTHOR(S) J. E. Pollard					
7. PERFORMING ORGANIZATION NAME(S) AND ADDRESS(ES) The Aerospace Corporation Technology Operations El Segundo, CA 90245				8. PERFORMING ORGANIZATION REPORT NUMBER TR-2000(8565)-10	
9. SPONSORING/MONITORING AGENCY NAME(S) AND ADDRESS(ES) Space and Missile Systems Center Air Force Materiel Command 2430 E. El Segundo Blvd. Los Angeles Air Force Base, CA 90245				10. SPONSORING/MONITORING AGENCY REPORT NUMBER SMC-TR-	
11. SUPPLEMENTARY NOTES					
12a. DISTRIBUTION/AVAILABILITY STATEMENT Approved for public release; distribution unlimited				12b. DISTRIBUTION CODE	
13. ABSTRACT (Maximum 200 words) Low-thrust maneuvers are evaluated by calculating changes in the orbital elements with pre-defined steering programs. Four pitch steering cases are considered, where the in-plane acceleration vector is (1) perpendicular to the orbit radius vector, (2) tangent to the orbit path, (3) perpendicular to the major axis of the ellipse, and (4) parallel to the major axis of the ellipse. Discontinuous thrusting is described using perigee- and apogee-centered burn arcs. Expressions are given for the secular rates of change of the orbital elements, which can be integrated numerically or in some instances solved in closed form to yield the ΔV and trip time. Maneuvers analyzed here include simultaneous eccentricity and inclination changes, adjusting the argument of perigee and right ascension of the ascending node (RAAN), phase shifting with RAAN control, and changes of the semimajor axis and eccentricity due to atmospheric drag. Mission applications are illustrated by orbit insertion at low, medium, and geosynchronous altitudes using chemical and electric propulsion, orbit disposal by re-entry or graveyarding, and controlling the separation distance between a target and a chase satellite in low Earth orbit.					
14. SUBJECT TERMS orbital maneuvers, low-thrust, electric propulsion, mission analysis				15. NUMBER OF PAGES 35	
				16. PRICE CODE	
17. SECURITY CLASSIFICATION OF REPORT UNCLASSIFIED	18. SECURITY CLASSIFICATION OF THIS PAGE UNCLASSIFIED	19. SECURITY CLASSIFICATION OF ABSTRACT UNCLASSIFIED	20. LIMITATION OF ABSTRACT		

Abstract

Low-thrust maneuvers are evaluated by calculating changes in the orbital elements with pre-defined steering programs. Four pitch steering cases are considered, where the in-plane acceleration vector is (1) perpendicular to the orbit radius vector, (2) tangent to the orbit path, (3) perpendicular to the major axis of the ellipse, and (4) parallel to the major axis of the ellipse. Discontinuous thrusting is described using perigee- and apogee-centered burn arcs. Expressions are given for the secular rates of change of the orbital elements, which can be integrated numerically or in some instances solved in closed form to yield the ΔV and trip time. Maneuvers analyzed here include simultaneous eccentricity and inclination changes, adjusting the argument of perigee and right ascension of the ascending node (RAAN), phase shifting with RAAN control, and changes of the semimajor axis and eccentricity due to atmospheric drag. Mission applications are illustrated by orbit insertion at low, medium, and geosynchronous altitudes using chemical and electric propulsion, orbit disposal by re-entry or graveyarding, and controlling the separation distance between a target and a chase satellite in low Earth orbit.

Acknowledgement

The author would like to thank George Chao of the Astrodynamics Department for calculating the spacecraft deceleration due to atmospheric drag. This project was supported in part by the Independent Research and Development program and by the Mission-Oriented Investigation and Experimentation program at The Aerospace Corporation.

Contents

Abstract.....	1
Acknowledgement.....	2
Introduction	9
Steering Programs and Secular Rates.....	9
Simultaneous Eccentricity and Inclination Changes.....	15
Adjusting the Argument of Perigee.....	18
Adjusting the Right Ascension of the Ascending Node.....	18
Adjusting the Orbital Phase with RAAN Compensation	20
Circularizing a GEO Transfer Orbit.....	21
MEO Insertion	25
Atmospheric Drag	27
LEO Insertion.....	29
Orbit Disposal.....	30
Drag Compensation for Co-Orbiting Satellites.....	32
References	37
Appendix 1	39

Figures

Figure 1. Orbital elements and components of acceleration f . The direction of f_r is radially outward, f_t is in-track, and f_s is cross-track.....	10
Figure 2. Perigee- and apogee-centered burn arcs are specified in units of eccentric anomaly E where $-\alpha \leq E \leq +\alpha$ or $180^\circ - \alpha \leq E \leq 180^\circ + \alpha$	12
Figure 3. Comparison of in-plane steering cases (1), (2), and (3) in a geosynchronous transfer orbit with an apogee altitude of 35,786 km and a perigee altitude of 185 km. Secular rates of change for a and e are calculated from Table 3 with $f = 3 \times 10^{-7}$ km/s ² , and with the burn arc given by α , as defined in Figure 2.....	13
Figure 4. Dependence of the function G on α , as defined in Table 3. Orbit parameters are the same as in Figure 3. Secular rates of change of i , Ω , and ω are proportional to G	15
Figure 5. Out-of-plane thrust angle for an inclination change with simultaneous circularization. Results are calculated from Eq. (9) with five different values of the initial eccentricity and with $\omega = 0^\circ$ or 180°	17
Figure 6. Velocity increment for an inclination change with simultaneous circularization using the out-of-plane thrust angles in Figure 5. Semimajor axis is constant at $a = 42,164$ km (24-hour period). Results are calculated from Eq. (5) with five different values of the initial eccentricity.....	17
Figure 7. Velocity increment for canceling apsidal rotation using case (4) steering with perigee- and apogee-centered burns specified by α . Results are calculated from Eq. (14) with average altitudes of 300, 700, and 1400 km.....	19
Figure 8. Velocity increment vs. trip time for a 45° relative RAAN shift at 1400-km altitude with $i = 50^\circ$ and $e = 0.001$. Three different values of the low-thrust acceleration are displayed. The end-point of each curve is when the drift time is zero.....	20
Figure 9. Velocity increment and trip time for orbital phase shifting at 600-km altitude with $i = 60^\circ$ and $f = 0.75 \times 10^{-7}$ km/s ² during two symmetrical 15-minute burns per revolution. Black symbols are with RAAN control, and white symbols are without RAAN control.	21
Figure 10. Orbital elements vs. time for a GTO-to-GEO transfer with an acceleration of $f = 3 \times 10^{-7}$ km/s ²	22
Figure 11. Velocity increment vs. trip time to reach GEO from a park orbit with a perigee radius of 15,000 km. Park apogee radius (km) and inclination ($^\circ$) are specified on the graph....	23
Figure 12. Satellite mass vs. trip time to reach GEO from an Atlas IIAS booster via a park orbit with a perigee radius of 15,000 km. Park apogee radius (km) and inclination ($^\circ$) are specified on the graph.....	24
Figure 13. Satellite mass vs. trip time to reach GEO from an Atlas IIAS booster via a park orbit with perigee radii of 15,000, 21,000, and 27,000 km.....	24
Figure 14. Satellite mass vs. trip time to reach GEO from an Atlas IIAS booster via a park orbit with a 24-hour period. Park perigee radius (km) and inclination ($^\circ$) are specified on the graph.	25

Figure 15. Spacecraft mass delivered by a medium launch vehicle to an elliptical park orbit at 27° inclination. Apogee radius is the independent variable, and the seven curves correspond to different perigee radii. The satellite is dropped off at an initial perigee altitude of 167 km, and the on-board chemical system (326 s specific impulse) raises the perigee radius to the values indicated.	26
Figure 16. Spacecraft mass delivered to a circular MEO altitude of 18,000 km at 27° inclination, plotted as a function of trip time. The six curves with symbols correspond to different values of the apogee.	27
Figure 17. Logarithm of atmospheric drag deceleration for circular orbits with $i = 33^\circ$ for a 130-kg spacecraft. The solar array is sun-pointing with an area of 2.9 m^2 , and the 1.0-m^3 spacecraft body is nadir-pointing. The atmospheric density model is MSIS90 at solar-maximum conditions.	28
Figure 18. Velocity increment vs. initial mean altitude for co-planar transfer to an 800-km circular orbit with three values for the spacecraft acceleration.	29
Figure 19. Trip time vs. initial mean altitude for co-planar transfer to an 800-km circular orbit with three values for the spacecraft acceleration.	30
Figure 20. De-orbiting from an 800-km circular orbit via apogee-centered burn arcs with $f = 0.75 \times 10^{-7} \text{ km/s}^2$. The velocity increment is 218 m/s, and 57 days are required to reach a mean altitude of 250 km.	31
Figure 21. Velocity increment vs. trip time for disposal from near-circular orbits with initial altitudes of 400-1600 km. The spacecraft acceleration is $f = 0.75 \times 10^{-7} \text{ km/s}^2$. The graveyard orbit has a circular altitude of 2000 km.	31
Figure 22. Changing the in-track separation between two co-orbiting satellites in the presence of atmospheric drag. Thrust acceleration of satellite 2 is $0.75 \times 10^{-7} \text{ km/s}^2$ during two symmetrical 15-minute burns per revolution. The ΔV for this maneuver is 3.94 m/s and the trip time is 1.96 days.	33
Figure 23. Controlling the separation distance between two co-orbiting satellites over a 1-year mission. Satellite 1 is passive, while satellite 2 (which has a 10% greater area-to-mass ratio) uses periodic thrusting to raise its altitude above that of satellite 1. The ΔV for the 1-year mission is 5.3 m/s.	33
Figure 24. Separation tolerance vs. cycle time for differential drag compensation by two co-orbiting satellites having area-to-mass ratios that differ by 10%. Results are displayed at four circular altitudes with solar maximum conditions.	35

Tables

Table 1. Rates of change of the orbital elements with E , where $\mu = 398,600.5 \text{ km}^3 \text{ s}^{-2}$	11
Table 2. In-plane (pitch) steering with four different choices for the in-plane acceleration vector, where $f_{12} \equiv \sqrt{(f_1)^2 + (f_2)^2} = f \cos \beta$	11
Table 3. Secular rates of change of the orbital elements with four different choices for the in-plane acceleration vector.....	14

Introduction*

Techniques for evaluating low-thrust orbital maneuvers are of interest because of the anticipated near-term use of electric propulsion for tasks with significant ΔV such as geosynchronous orbit insertion and satellite disposal from low Earth orbit. Convenient analytical techniques are needed by mission planners to compare the ΔV and trip time in proposed orbit transfer scenarios. The 1961 paper by Edelbaum¹ presented optimal steering algorithms for continuous thrusting in near-circular orbits, which served as the starting point for many subsequent analyses to determine a steering program that minimizes trip time or propellant mass.²⁻⁹ However, these methods tend to be computationally intensive and may be more elaborate than is needed for the first phase of a trade study. In addition, designing a trajectory to minimize the trip time could turn out to be impractical, because the satellite may not be able to execute the optimal steering programs that have been envisioned for dedicated orbit transfer vehicles.

We present calculations of the velocity increment and trip time using simple pre-defined steering programs and an averaging technique that ignores the short-term variation of the orbital elements. This is based on the low-thrust formulation of Burt¹⁰, in which the secular rate of change of one element is calculated by holding the others constant over one revolution. Burt's approach is extended here to the case of discontinuous acceleration by analyzing perigee- and apogee-centered burn arcs. Secular rates of change are derived analytically and integrated numerically to obtain the history of each element throughout the maneuver. Closed form solutions for the ΔV and trip time are possible in some cases. This allows a rapid assessment of design options for placing a satellite into the desired orbit, prior to a more complete optimization when the trade-space has been narrowed. After introducing the steering programs and secular rate expressions we present an analysis of simultaneous eccentricity and inclination changes, adjusting the argument of perigee and right ascension of the ascending node (RAAN), phase adjustments with RAAN control, and the effect of atmospheric drag on semimajor axis and eccentricity. Examples of mission applications include insertion at low, medium, and geosynchronous altitudes using chemical and electric propulsion, orbit disposal by re-entry or graveyarding, and controlling the separation distance between a target and a chase satellite.

Steering Programs and Secular Rates

In Burt's nomenclature f is the thrust per unit mass (i.e., acceleration) having three components that are defined using in-track, cross-track, and radial coordinates as shown in Figure 1. Here, f_1 is directed outward along the radius vector, f_2 is in the orbit plane and normal to the radius vector, f_3 is normal to the orbit plane in the direction of the angular momentum vector, and the magnitude of the

* This report is a synthesis of three conference publications:

J. E. Pollard, "Simplified approach for assessment of low-thrust elliptical orbit transfers," Papager IEPC-97-160, 25th International Electric Propulsion Conference, 24-28 Aug 1997, Cleveland, Ohio.

J. E. Pollard, "Evaluation of low-thrust orbital maneuvers," Paper AIAA-98-3486, 34th Joint Propulsion Conference, 13-15 July 1998, Cleveland, Ohio.

J. E. Pollard, "Low-thrust maneuvers for LEO and MEO missions," Paper AIAA-99-2870, 35th Joint Propulsion Conference, 20-24 June 1999, Los Angeles, California.

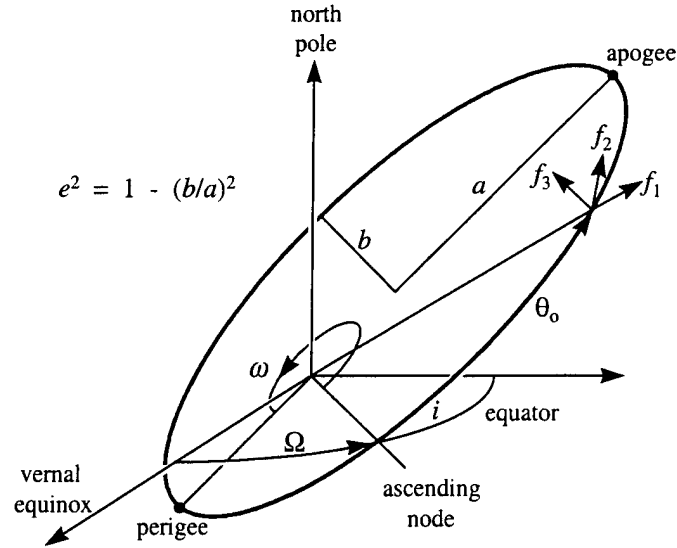


Figure 1. Orbital elements and components of acceleration f . The direction of f_1 is radially outward, f_2 is in-track, and f_3 is cross-track.

acceleration is $f = \sqrt{(f_1)^2 + (f_2)^2 + (f_3)^2}$. Table 1 shows the rates of change of the semimajor axis a , eccentricity e , inclination i , right ascension of the ascending node (RAAN) Ω , and argument of perigee ω as functions of eccentric anomaly E . These rates are derived from the Lagrange planetary equations listed in Reference 10. Elements a and e are affected by the in-plane components f_1 and f_2 , while i and Ω are affected by the out-of-plane component f_3 , and ω is affected by all three components. Specifying f_1 , f_2 , and f_3 as functions of E defines the steering program and determines the relative rates of change of the elements. Table 2 lists $f_1(E)$ and $f_2(E)$ in four different pitch steering cases, where the in-plane acceleration vector is (1) perpendicular to the orbit radius vector, (2) tangent to the orbit path, (3) perpendicular to the major axis of the ellipse, and (4) parallel to the major axis of the ellipse. Cases (1) and (2) are used for concurrent adjustments of a and e , and they are identical in the limit of small e . Case (3) can change e at a constant value of a , and case (4) adjusts ω while a and e are unaffected.

Discontinuous thrusting is described using perigee- or apogee-centered burns over an arc specified by α , as shown in Figure 2. The magnitude of f and the magnitude of the out-of-plane thrust angle β are held constant during each burn arc, and the in-plane and out-of-plane components of acceleration are

$$f_{12} = \sqrt{(f_1)^2 + (f_2)^2} = f \cos|\beta|, \quad f_3 = f \sin|\beta|. \quad (1)$$

When both perigee- and apogee-centered burns are used, then the sign of β is reversed twice per revolution at minor axis crossings to improve the efficiency of plane change maneuvers. This requires cyclic yaw maneuvers or alternate firing of canted thrusters on opposite sides of the vehicle. Although it is feasible to introduce a slowly varying β (as is done in Reference 1), this yields little or no benefit for the examples presented here. A slowly varying acceleration, such as for the case of constant thrust and decreasing vehicle mass, can also be incorporated into the numerical analysis if needed.

Table 1. Rates of change of the orbital elements with E , where $\mu = 398,600.5 \text{ km}^3 \text{ s}^{-2}$.

$\frac{da}{dE}$	$\frac{2a^3}{\mu} (f_1 e \sin E + f_2 \sqrt{1-e^2})$
$\frac{de}{dE}$	$\frac{a^2}{\mu} [f_1 (1-e^2) \sin E + f_2 \sqrt{1-e^2} (2 \cos E - e - e \cos^2 E)]$
$\frac{di}{dE}$	$\frac{a^2}{\mu} f_3 (1-e \cos E) \left[\frac{(\cos E - e) \cos \omega}{\sqrt{1-e^2}} - \sin E \sin \omega \right]$
$\frac{d\Omega}{dE}$	$\frac{a^2}{\mu} f_3 \frac{1-e \cos E}{\sin i} \left[\frac{(\cos E - e) \sin \omega}{\sqrt{1-e^2}} + \sin E \cos \omega \right]$
$\frac{d\omega}{dE}$	$\frac{a^2}{\mu} \left\{ \frac{1}{e} \left[-f_1 \sqrt{1-e^2} (\cos E - e) + f_2 (2-e^2 - e \cos E) \sin E \right] - f_3 (1-e \cos E) \cot i \left[\frac{(\cos E - e) \sin \omega}{\sqrt{1-e^2}} + \sin E \cos \omega \right] \right\}$

Table 2. In-plane (pitch) steering with four different choices for the in-plane acceleration vector, where $f_{12} \equiv \sqrt{(f_1)^2 + (f_2)^2} = f \cos \beta$.

	(1) Perpendicular to the orbit radius vector	(2) Tangent to the orbit path	(3) Perpendicular to the major axis of the ellipse	(4) Parallel to the major axis of the ellipse
$f_1(E)$	0	$\frac{f_{12} e \sin E}{\sqrt{1-e^2 \cos^2 E}}$	$\frac{f_{12} \sqrt{1-e^2} \sin E}{1-e \cos E}$	$\frac{f_{12} (\cos E - e)}{1-e \cos E}$
$f_2(E)$	f_{12}	$f_{12} \sqrt{\frac{1-e^2}{1-e^2 \cos^2 E}}$	$\frac{f_{12} (\cos E - e)}{1-e \cos E}$	$\frac{-f_{12} \sqrt{1-e^2} \sin E}{1-e \cos E}$

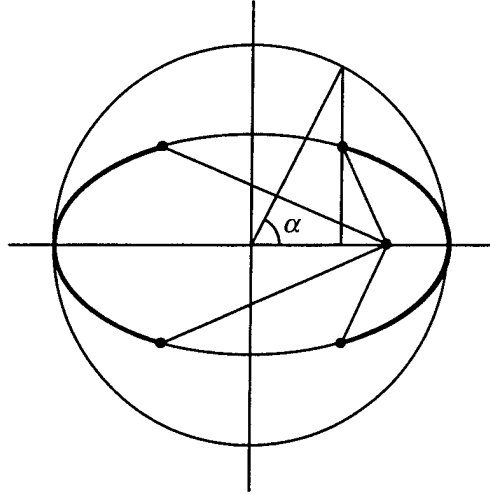


Figure 2. Perigee- and apogee-centered burn arcs are specified in units of eccentric anomaly E where $-\alpha \leq E \leq +\alpha$ or $180^\circ - \alpha \leq E \leq 180^\circ + \alpha$.

The selected steering program from Table 2 is applied to the rates of change of the orbital elements with respect to E in Table 1, and the resulting expressions are integrated over the burn arc to determine the change in each element during one revolution. Dividing these results by the orbit period τ (see Appendix 1) yields expressions for the secular rates of change of the elements, which are listed in Table 3. These rates can be integrated numerically or solved in some instances to yield the ΔV and trip time in closed form. The formula in Table 3 for the buildup rate of ΔV is derived from the burn duration per revolution,

$$t_{burn} = 2 \sqrt{a^3 / \mu} (\alpha + \sigma e \sin \alpha), \quad (2)$$

where the parameter σ equals -1 for perigee burns and $+1$ for apogee burns.

Figure 3 compares secular rates for the different steering programs as a function of burn arc. When the burn arc is small the steering programs for cases (1), (2), and (3) become equivalent, and hence there is a convergence in the secular rates of change of a and e in the limit of small α . Case (2) steering is more efficient than case (1) for changing a by either apogee- or perigee-centered burns, while changing e is better performed by case (1) in apogee burns and by case (2) in perigee burns. Case (3) has the in-plane acceleration perpendicular to the major axis of the ellipse, which is rather ineffective for changing a , but for continuous thrusting ($\alpha = 180^\circ$) it can efficiently change e while keeping a constant. Case (4) has the in-plane acceleration parallel to the major axis of the ellipse, which gives no change in a , e , i , or Ω , but (unlike the other in-plane cases) does produce a change in ω . Only the out-of-plane component of acceleration f_3 affects the orientation of the orbit plane, and hence the four in-plane steering cases give the same results for i and Ω in Table 3. The function $G(\sigma, \alpha, e)$ appears in the rates of change of i , Ω , and ω , and the graph of G in Figure 4 shows that apogee burns are much more effective than perigee burns for adjusting these elements. This graph also indicates that plane changing at a fixed yaw angle is inefficient when the apogee burn arc extends over more than half of the ellipse ($\alpha > 90^\circ$). A maneuver to change i is best performed with $\omega = 0^\circ$ or 180° , because the rate of change of i is proportional to $\cos \omega$. Similarly, a maneuver to change Ω is best performed with $\omega = 90^\circ$ or 270° . Due to the i -dependence of the formulas in Table 3, the rates of change of Ω and ω become infinite as the

inclination approaches zero, but the rate of change of the longitude of periapsis ($\Pi \equiv \Omega + \omega$) remains finite.

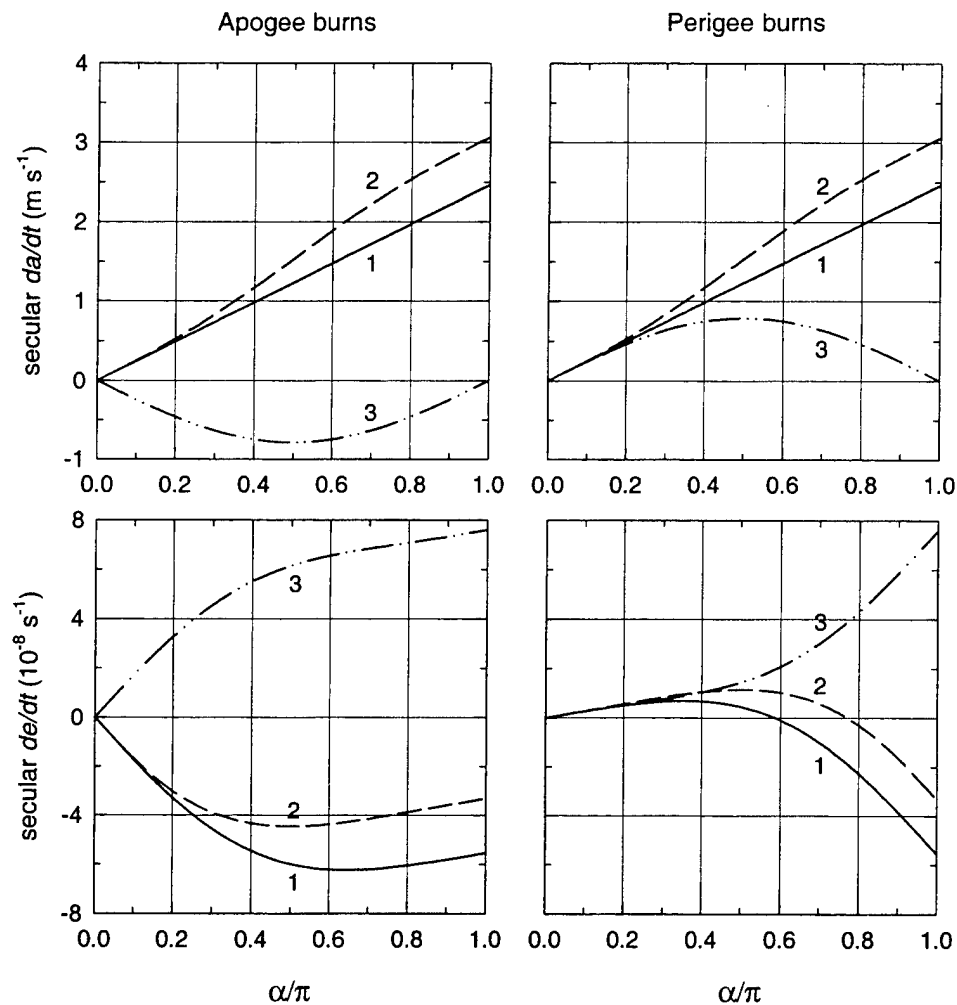


Figure 3. Comparison of in-plane steering cases (1), (2), and (3) in a geosynchronous transfer orbit with an apogee altitude of 35,786 km and a perigee altitude of 185 km. Secular rates of change for a and e are calculated from Table 3 with $f = 3 \times 10^{-7} \text{ km/s}^2$, and with the burn arc given by α , as defined in Figure 2.

Table 3. Secular rates of change of the orbital elements with four different choices for the in-plane acceleration vector.

	(1) Perpendicular to the orbit radius vector	(2) Tangent to the orbit path	(3) Perpendicular to the major axis of the ellipse	(4) Parallel to the major axis of the ellipse
$\frac{da}{dt}$	$\frac{2f_{12}}{\pi} \sqrt{\frac{a^3}{\mu} (1-e^2)} \alpha$	$\frac{2f_{12}}{\pi} \sqrt{\frac{a^3}{\mu}} \int_0^\alpha \sqrt{1-e^2 \cos^2 E} dE$	$-\frac{2\sigma f_{12}}{\pi} \sqrt{\frac{a^3}{\mu}} (1-e^2) \sin \alpha$	0
$\frac{de}{dt}$	$-\frac{f_{12}}{2\pi} \sqrt{\frac{a}{\mu}} (1-e^2) (4\sigma \sin \alpha + 3e\alpha + e \cos \alpha \sin \alpha)$	$\frac{2f_{12}}{\pi} \sqrt{\frac{a}{\mu}} (1-e^2) H(\sigma, \alpha)$	$\frac{f_{12}}{2\pi} \sqrt{\frac{a}{\mu}} (1-e^2) (4\sigma e \sin \alpha + 3\alpha + \cos \alpha \sin \alpha)$	0
$\frac{di}{dt}$	$-\frac{f_3}{2\pi} \sqrt{\frac{a}{\mu}} \cos \omega G(\sigma, \alpha, e)$	same as (1)	same as (1)	same as (1)
$\frac{d\Omega}{dt}$	$-\frac{f_3}{2\pi} \sqrt{\frac{a}{\mu}} \frac{\sin \omega}{\sin i} G(\sigma, \alpha, e) + N(a, e, i)$	same as (1)	same as (1)	same as (1)
$\frac{d\omega}{dt}$	$\frac{f_3}{2\pi} \sqrt{\frac{a}{\mu}} \cot i \sin \omega G(\sigma, \alpha, e) + A(a, e, i)$	same as (1)	same as (1)	$\left[\frac{1}{2\pi} \sqrt{\frac{a}{\mu}} f_{12} \frac{\sqrt{1-e^2}}{e} (-2\sigma e \sin \alpha - 3\alpha + \cos \alpha \sin \alpha) + f_3 \cot i \sin \omega G(\sigma, \alpha, e) + A(a, e, i) \right]$
$\frac{d\Delta V}{dt}$	$\frac{1}{\pi} \sqrt{(f_{12})^2 + (f_3)^2} (\alpha + \sigma e \sin \alpha)$	same as (1)	same as (1)	same as (1)

Apogee burns have $\sigma = +1$, perigee burns have $\sigma = -1$. Expressions for the nodal regression rate $N(a, e, i)$ and apsidal rotation rate $A(a, e, i)$ are listed in Appendix 1.

$$G(\sigma, \alpha, e) \equiv \frac{2\sigma \sin \alpha (1+e^2) + 3e\alpha + e \cos \alpha \sin \alpha}{\sqrt{1-e^2}}, \quad H(\sigma = -1, \alpha) \equiv \int_0^\alpha \frac{\cos E (1-e \cos E)}{\sqrt{1-e^2 \cos^2 E}} dE, \quad H(\sigma = +1, \alpha) \equiv \int_\pi^{\pi+\alpha} \frac{\cos E (1-e \cos E)}{\sqrt{1-e^2 \cos^2 E}} dE$$

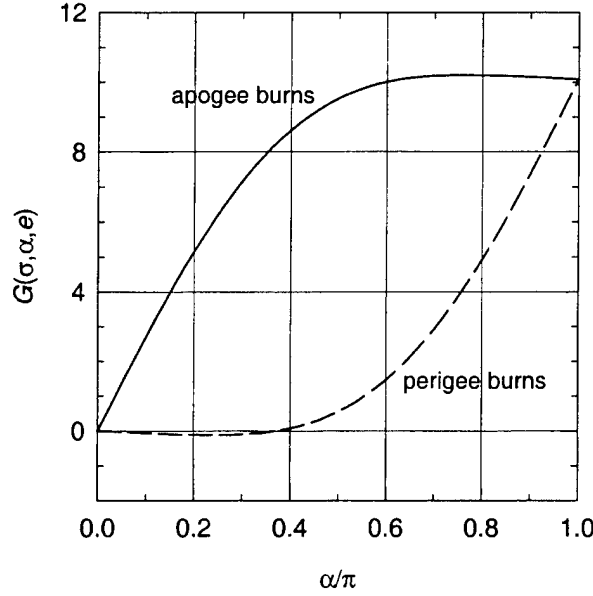


Figure 4. Dependence of the function G on α , as defined in Table 3. Orbit parameters are the same as in Figure 3. Secular rates of change of i , Ω , and ω are proportional to G .

Earth's gravitational field has a perturbing influence on Ω and ω that is expressed in Table 3 by the nodal regression rate N and apsidal rotation rate A . Expressions for these rates taken from Appendix 1 are added to the secular rates of change of Ω and ω due to thrusting. Apsidal rotation is a concern for elliptical orbit transfers that involve plane changing, because ω tends to drift away from the optimal value (e.g., $\omega = 0^\circ$ for a Δi maneuver). The numerical examples in this report take account of Earth's oblateness (J_2 term), but ignore other perturbations such as lunar-solar gravitation, solar radiation pressure, and higher order terms in the geopotential. The effects of satellite eclipsing and variable acceleration are also neglected.

Simultaneous Eccentricity and Inclination Changes

Adjusting e at constant semimajor axis is accomplished with in-plane acceleration perpendicular to the major axis of the ellipse, namely case (3) steering. When perigee- and apogee-centered burns occur on each revolution, the secular rate of change of e and the buildup rate of ΔV are

$$\left| \frac{de}{dt} \right| = \frac{f \cos|\beta|}{\pi} \sqrt{\frac{a}{\mu} (1 - e^2)} (3\alpha + \cos\alpha \sin\alpha), \quad (3)$$

$$\frac{d\Delta V}{dt} = \frac{2\alpha f}{\pi} \quad (4)$$

Here the maximum value of the burn arc is $\alpha = 90^\circ$, because both perigee and apogee burns are used. Integrating Eqs. (3) and (4) gives the velocity increment and trip time,

$$\Delta V = \frac{2 \alpha f \Delta t}{\pi} = \sqrt{\frac{\mu}{a}} \frac{2 \alpha |\arcsin e_1 - \arcsin e_2|}{\cos|\beta| (3 \alpha + \cos \alpha \sin \alpha)}. \quad (5)$$

The limiting cases of impulsive thrust (small α) and continuous thrust ($\alpha = 90^\circ$) can be compared using Eq. (5), and the result is

$$\Delta V_{cont} = \frac{4}{3} \Delta V_{imp}. \quad (6)$$

Hence the low-thrust eccentricity change needs a 33% greater ΔV than the corresponding impulsive maneuver.

We next evaluate the inclination change that occurs along with the change of eccentricity. Under the assumption that the sign of β reverses at minor axis crossings, the secular rate of change of i is

$$\left| \frac{di}{dt} \right| = \frac{f \sin|\beta|}{\pi} \sqrt{\frac{a}{\mu}} |\cos \omega| \sin \alpha \frac{2(1+e^2)}{\sqrt{1-e^2}}. \quad (7)$$

Adjusting the inclination by this method is efficient only when perigee and apogee are close to the line of nodes, namely when $\omega \approx 0^\circ$ or 180° . Dividing Eq. (7) by Eq. (3) gives the rate of change of i with respect to e ,

$$\left| \frac{di}{de} \right| = \frac{2 \tan|\beta| |\cos \omega| \sin \alpha}{3 \alpha + \cos \alpha \sin \alpha} \frac{1+e^2}{1-e^2}. \quad (8)$$

Integrating Eq. (8) between the initial and final conditions under the assumption that ω is constant gives an expression for the out-of-plane thrust angle β that causes i and e to reach their target values simultaneously:

$$\tan|\beta| = \left| \frac{(i_2 - i_1)(3 \alpha + \cos \alpha \sin \alpha)}{2 \cos \omega \sin \alpha \left[\ln \left(\frac{e_2 + 1}{e_2 - 1} \frac{e_1 - 1}{e_1 + 1} \right) - e_2 + e_1 \right]} \right|. \quad (9)$$

The argument of perigee ω will vary during the orbit transfer due to the natural drift and because e may approach zero. However, Eq. (9) still gives a good estimate of the desired thrust angle. Figure 5 shows results for circularization with an inclination change that are applicable at any value of the semimajor axis. The ΔV for circularization with an inclination change can be calculated from Eq. (5) using the β values from Eq. (9). Figure 6 applies to an orbit having a 24-hour period, and it shows that for small eccentricities ($e < 0.1$) the ΔV is nearly linear in Δi , and it approximates that of a pure inclination change. For large eccentricities ($e > 0.6$) the dependence of ΔV on Δi is less steep, because performing part of the inclination change at higher altitudes improves the maneuver efficiency.

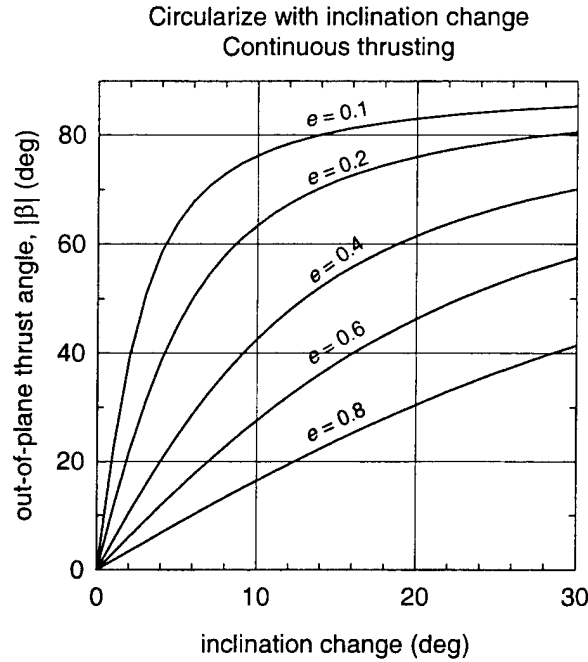


Figure 5. Out-of-plane thrust angle for an inclination change with simultaneous circularization. Results are calculated from Eq. (9) with five different values of the initial eccentricity and with $\omega = 0^\circ$ or 180° .

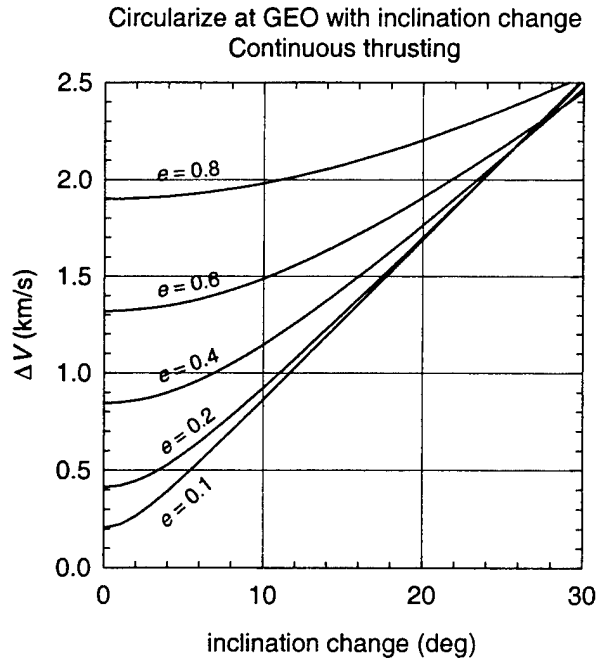


Figure 6. Velocity increment for an inclination change with simultaneous circularization using the out-of-plane thrust angles in Figure 5. Semimajor axis is constant at $a = 42,164$ km (24-hour period). Results are calculated from Eq. (5) with five different values of the initial eccentricity.

Adjusting the Argument of Perigee

Changing ω while holding a and e constant is performed using $\beta = 0^\circ$ and case (4) steering with the in-plane acceleration vector parallel to the major axis of the ellipse. Assuming that perigee- and apogee-centered burns occur on each revolution, the secular rate of change of ω is

$$\frac{d\omega}{dt} = \frac{\pm f}{\pi} \sqrt{\frac{a}{\mu}} \frac{\sqrt{1-e^2}}{e} (-3\alpha + \cos\alpha \sin\alpha) + A, \quad (10)$$

where A is the natural rate of apsidal rotation. By integrating Eq. (10) we obtain the velocity increment and trip time,

$$\Delta V = \frac{2\alpha f \Delta t}{\pi} = \frac{2\alpha \Delta\omega}{\text{sgn}(\Delta\omega) \sqrt{\frac{a}{\mu}} \frac{\sqrt{1-e^2}}{e} (3\alpha - \cos\alpha \sin\alpha) + \frac{\pi A}{f}} \quad (11)$$

where $\Delta\omega = \omega_2 - \omega_1$. Here ΔV depends on f because of the apsidal rotation term in Eq. (10). If the direction of the desired change in ω is opposite to the natural drift, then the maneuver is feasible only if the magnitude of the first term on the r.h.s. of Eq. (10) is greater than A . On the other hand, if the natural drift rate is negligible compared with the rate of change due to thrusting, then the velocity increment is

$$\Delta V = \sqrt{\frac{\mu}{a}} \frac{e}{\sqrt{1-e^2}} \frac{2\alpha |\Delta\omega|}{3\alpha - \cos\alpha \sin\alpha}, \quad (12)$$

which is independent of f . If we use Eq. (12) to compare the limiting cases of impulsive thrust (small α) and continuous thrust ($\alpha = 90^\circ$) for adjusting ω the result is

$$\Delta V_{\text{cont}} = \frac{2}{3} \Delta V_{\text{imp}}. \quad (13)$$

This is a rare example of a low-thrust maneuver that has a smaller ΔV than the corresponding impulsive maneuver! Another way of illustrating this is by setting Eq. (10) equal to zero to obtain the velocity increment for canceling apsidal rotation for a time interval Δt , namely

$$\Delta V = \sqrt{\frac{\mu}{a}} \frac{e}{\sqrt{1-e^2}} \frac{2\alpha |A| \Delta t}{3\alpha - \cos\alpha \sin\alpha}, \quad (14)$$

which is depicted in Figure 7 as a function of the burn arc angle. The limiting cases of impulsive (small α) and continuous maneuvers ($\alpha = 90^\circ$) are again related by Eq. (13).

Adjusting the Right Ascension of the Ascending Node

Changing Ω at a rate different from the natural drift rate is done using out-of-plane thrusting with burn arcs centered about the apices (i.e., the maximum and minimum latitude points). In near-

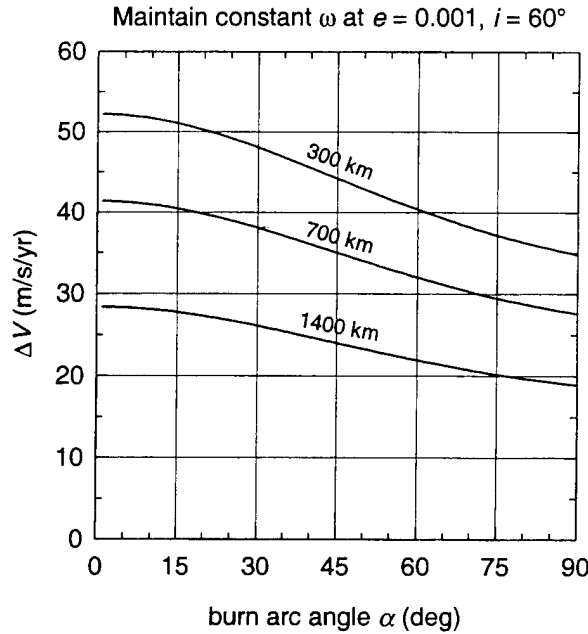


Figure 7. Velocity increment for canceling apsidal rotation using case (4) steering with perigee- and apogee-centered burns specified by α . Results are calculated from Eq. (14) with average altitudes of 300, 700, and 1400 km.

circular orbits the velocity increment for adjusting the RAAN relative to a reference orbit is where

$$\Delta V = \frac{\pi}{2} \sqrt{\frac{\mu}{a}} \sin i |\Delta\Omega|, \quad (15)$$

continuous out-of-plane thrusting at fixed altitude is assumed, and the direction of thrust reverses twice per orbit at the line of nodes. Performing plane changes in this manner is very costly in terms of propellant. The preferred method for adjusting Ω takes advantage of the natural rate of nodal regression and its dependence on altitude. Transferring to lower or higher altitude changes the regression rate relative to the initial orbit, and a shift in Ω will build up with time. After loitering in the drift orbit the spacecraft returns to the initial orbit by reversing the direction of the in-plane acceleration. Figure 8 compares the trade-off between ΔV and trip time for a 45° RAAN adjustment by impulsive maneuvers and by low-thrust spiral transfers with three different values for the spacecraft acceleration. This example assumes case (1) steering with both perigee- and apogee-centered burns and continuous in-plane thrusting ($\alpha = 90^\circ$, $\beta = 0^\circ$). Increasing the acceleration provides a more efficient transfer, as indicated by the curves for $f = 0.5, 1.0$, and $2.0 \times 10^{-7} \text{ km/s}^2$. The minimum trip time for a given f is achieved when the drift time is zero, namely when thrusting occurs throughout the entire maneuver, as indicated by the end point of each curve. One application of Figure 8 is for a LEO constellation having four orbital planes at $i = 50^\circ$ with the RAAN spaced in equal increments ($\Delta\Omega = 45^\circ$). A satellite that has failed prematurely could be replaced by a spare from an adjacent plane, assuming that the long trip time for this plane change is a better option than putting the replacement on another launch vehicle.

Phase shifts are performed by satellites during the build-up of constellations and to replace a failed spacecraft with an on-orbit spare. The strategy is to use in-plane thrusting perpendicular to the orbit radius to increase or decrease the altitude until half of the desired phase shift is accumulated.

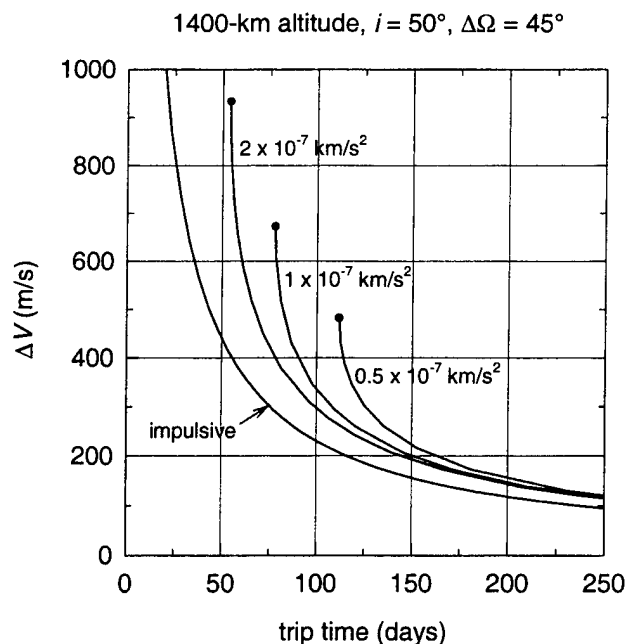


Figure 8. Velocity increment vs. trip time for a 45° relative RAAN shift at 1400-km altitude with $i = 50^\circ$ and $e = 0.001$. Three different values of the low-thrust acceleration are displayed. The end-point of each curve is when the drift time is zero.

Adjusting the Orbital Phase with RAAN Compensation

Reversing the thrust direction returns the satellite to the initial altitude at the target phase. As usual, there is an inverse relation between trip time and ΔV . Loitering in a drift orbit between the inbound and outbound maneuvers is useful if a reduced ΔV and longer trip time are preferred, but the following example assumes there is no loitering. A complication arises at low and medium altitudes because a shift of the RAAN relative to the non-thrusting reference orbit occurs simultaneously with the desired phase shift. The RAAN shift can be compensated by including an out-of-plane thrust component that is constant in magnitude but reverses sign at the line of nodes, which occurs near the minor axis crossings when $\omega \approx 90^\circ$ or 270° . Figure 9 shows the ΔV and trip time for phase shifting in a near-circular orbit with and without RAAN control. Two symmetrical burns are performed on each revolution centered about the apices (maximum latitude points), with the direction of the out-of-plane thrust component reversing between burns, either by cyclic yaw maneuvers or by alternate firing of canted thrusters. The out-of-plane thrust angle β is chosen so that the RAAN is identical to that of the reference orbit at the end of the phase change maneuver. The out-bound and in-bound burn times are slightly different in order to compensate for differential drag during the maneuver (see below for a discussion of drag compensation). For a 180° phase shift, the use of RAAN control increases the ΔV and the trip time by 46% and requires an out-of-plane thrust angle of $\beta = \pm 62^\circ$. Without RAAN control, a 180° phase shift in LEO would change the RAAN by about 0.3° relative to a non-thrusting reference orbit.

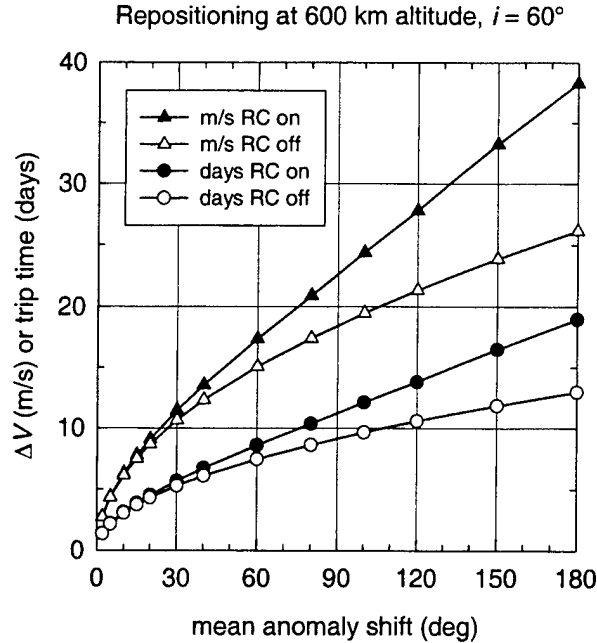


Figure 9. Velocity increment and trip time for orbital phase shifting at 600-km altitude with $i = 60^\circ$ and $f = 0.75 \times 10^{-7} \text{ km/s}^2$ during two symmetrical 15-minute burns per revolution. Black symbols are with RAAN control, and white symbols are without RAAN control.

Circularizing a GEO Transfer Orbit

Suppose that a spacecraft is in an elliptical transfer orbit with an apogee altitude of 35,786 km, a perigee altitude of 185 km, and $i = 28.5^\circ$. A transfer to geosynchronous equatorial orbit (GEO) is accomplished by increasing the semimajor axis while bringing the eccentricity and inclination to zero. Figure 10 shows the history of the orbital elements during a typical mission. The assumed acceleration of $f = 3 \times 10^{-7} \text{ km/s}^2$ corresponds to a thruster producing 50 mN per kW of input power and a satellite having a power-to-mass ratio of 6 W/kg. The first segment of the transfer uses case (1) steering, apogee-centered burns with $\alpha = 108^\circ$, and an out-of-plane thrust angle of $\beta = +40.4^\circ$, which takes the semimajor axis to the target value of 42,164 km in 97 days. The second segment uses case (3) steering, continuous thrust, and $\beta = \pm 26.0^\circ$ to drive the eccentricity and inclination to zero in 23 days while the semimajor axis remains constant. The out-of-plane thrust angle for the second segment is calculated from Eq. (9). Values for α and β in the first segment are chosen to minimize the product of the total velocity increment and total trip time ($\Delta V \times \Delta t$) for the selected steering program. This is equivalent to finding the “knee” of the ΔV vs. Δt curve that yields a favorable trade-off between propellant mass and trip time. During the first segment, the argument of perigee ω changes because of the natural drift and because of the out-of-plane thrust component. To get around this problem we initialize at $\omega = -13.5^\circ$ and drift toward $\omega \approx -1^\circ$ as i approaches zero, which maintains a good geometrical efficiency for inclination changing throughout the mission. The total ΔV is 2.50 km/s with a 120-day trip time for this low-thrust transfer, compared with an impulsive (high thrust) ΔV of 1.84 km/s.

We next consider a transfer to GEO by a combination of low-thrust and impulsive maneuvers. In this scenario the launch vehicle places the satellite in an orbit with a variable apogee radius, a perigee

altitude of 185 km, and $i = 27^\circ$. The on-board chemical system then fires at apogee to reach a park orbit having a perigee radius of 15,000 km and a variable inclination. This perigee radius is selected to minimize exposure to high-energy protons during the low-thrust part of the mission. The spacecraft travels to GEO by the same approach as in Figure 10 at an acceleration of $f = 3 \times 10^{-7} \text{ km/s}^2$. The burn arc angle α , the out-of-plane thrust angle β , and the initial ω are chosen to minimize $\Delta V \times \Delta t$ as in the previous example. Figure 11 shows the velocity increment as a function of trip time for the low-thrust maneuver with the park apogee radius and inclination displayed parametrically. For a given apogee radius, ΔV is an increasing function of trip time, governed by the choice of park inclination (more Δi means a longer trip and greater ΔV). For a given park inclination, ΔV can be either a decreasing or

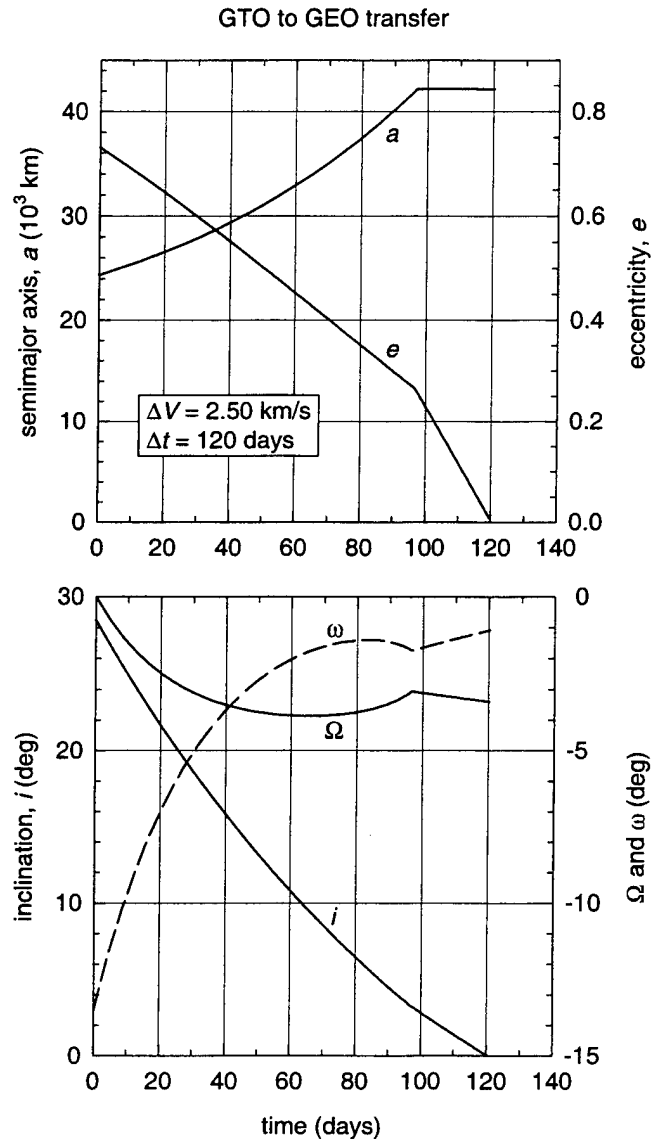


Figure 10. Orbital elements vs. time for a GTO-to-GEO transfer with an acceleration of $f = 3 \times 10^{-7} \text{ km/s}^2$.

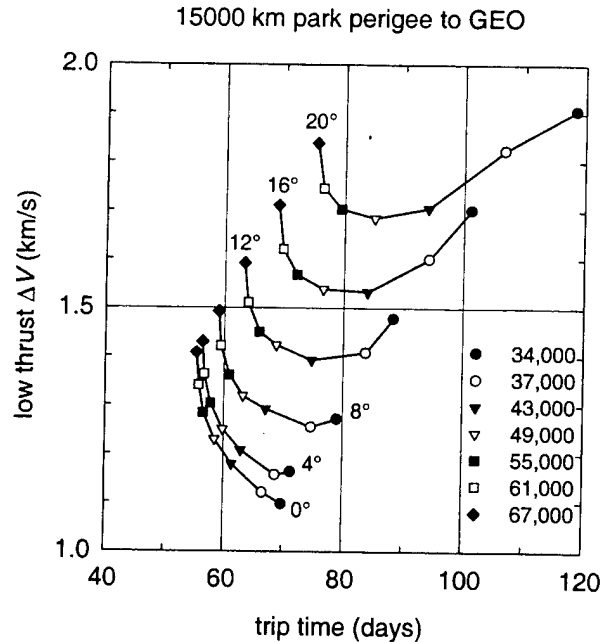


Figure 11. Velocity increment vs. trip time to reach GEO from a park orbit with a perigee radius of 15,000 km. Park apogee radius (km) and inclination ($^{\circ}$) are specified on the graph.

increasing function of trip time depending on park apogee radius. It may be surprising to see that the ΔV to GEO can *increase* as the park apogee radius increases. This is because the park orbit eccentricity increases with apogee radius, and the higher ΔV for circularization more than offsets the lower ΔV needed to change a . One also finds that an intermediate apogee radius gives the minimum ΔV for a given inclination (e.g., 43,000 km at $i = 12^{\circ}$), due to the penalty associated with plane changing at lower radii.

Typically the mission planner seeks to maximize payload mass at GEO for a given trip time, which is not necessarily achieved by minimizing the low-thrust ΔV . The spacecraft mass that the launch vehicle can deliver to the park orbit depends on apogee radius and inclination (i.e., decreased mass if the orbit is higher and less inclined). Hence, the results in Figure 11 must be combined with performance figures for the launch vehicle and the spacecraft chemical system to optimize the mass-vs.-time trade-off to GEO. This is depicted in Figure 12 for the case of an Atlas IIAS booster with the park perigee radius fixed at 15,000 km. On-board propulsion systems are assumed to have specific impulses of 314 s (chemical) and 1600 s (electric). Trip times reported here do not include the time from lift-off to the end of the chemical orbit transfer, which is typically 2-7 days. Several interesting trends are evident in Figure 12. If the park orbit is confined to $i = 0^{\circ}$ (equatorial), then the best apogee radius is around 55,000 km, and the satellite mass at GEO is 2411 kg with a 56-day trip time (an improvement of at least 400 kg over an all-chemical propulsion system). Further mass gains are possible if the spacecraft is capable of changing the inclination during the low-thrust segment of the mission. A satellite mass of 2604 kg and a 75-day trip time are achieved when the park inclination is $i = 12^{\circ}$ and the apogee radius is 43,000 km. No additional benefit is obtained for park inclinations greater than $i = 20^{\circ}$. Similarly, if the park perigee is fixed at 15,000 km, then apogee radii greater than 60,000 km are to be avoided, because they give a sharp reduction in GEO mass with little or no savings in trip time.

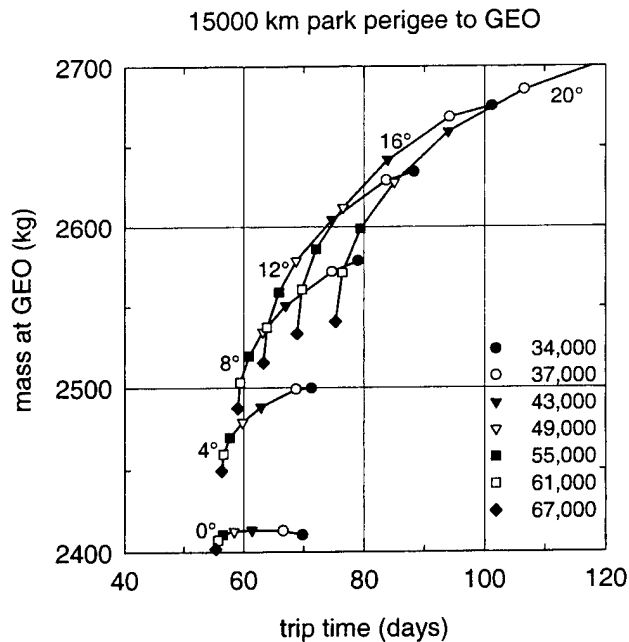


Figure 12. Satellite mass vs. trip time to reach GEO from an Atlas IIAS booster via a park orbit with a perigee radius of 15,000 km. Park apogee radius (km) and inclination ($^{\circ}$) are specified on the graph.

Some missions may require shorter trip times than are depicted in Figure 12, and this can be achieved using park perigee radii greater than 15,000 km. Figure 13 shows the same data as in Figure

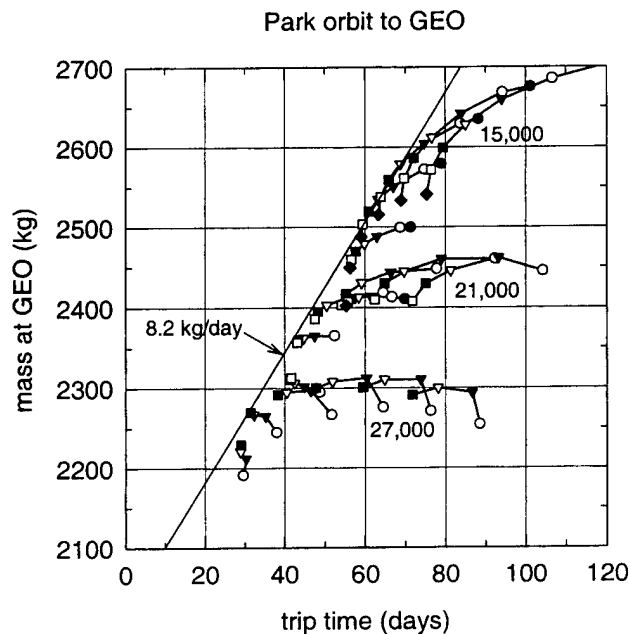


Figure 13. Satellite mass vs. trip time to reach GEO from an Atlas IIAS booster via a park orbit with perigee radii of 15,000, 21,000, and 27,000 km.

12, along with results for two cases with higher perigee radii. The trade-off between trip time and mass at GEO indicated by the line in Figure 10 is 8.2 kg/day for masses in the range of 2200-2600 kg. The trip time of 30-70 days assumes an acceleration of $f = 3 \times 10^{-7} \text{ km/s}^2$ and a favorable choice of apogee radius and inclination at each park perigee radius. Another important case is the transfer to GEO from a park orbit having a variable perigee radius, a variable inclination, and a 24-hour period so that the transfer is performed within view of a single ground station.¹¹ Figure 14 shows the mass at GEO vs. trip time using the same set of performance assumptions as in Figure 12 with $f = 3 \times 10^{-7} \text{ km/s}^2$. The best choice of park inclination is $i \approx 4^\circ$ for perigee radii of 21,000-33,000 km, while $i \approx 8^\circ$ is preferable for radii of 15,000-21,000 km. With these inclination choices, the mass benefit from starting the low-thrust orbit transfer at a lower perigee radius amounts to 7.7 kg per extra day of trip time.

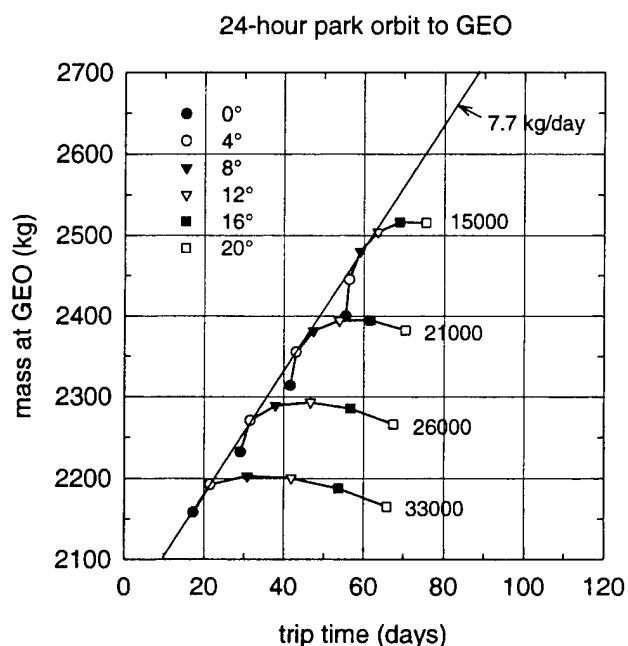


Figure 14. Satellite mass vs. trip time to reach GEO from an Atlas IIAS booster via a park orbit with a 24-hour period. Park perigee radius (km) and inclination ($^\circ$) are specified on the graph.

MEO Insertion

In the next example, the satellite is launched into an initial orbit having a variable apogee altitude, a perigee altitude of 167 km, and an inclination of 27° . The on-board chemical propulsion system fires at apogee to raise the park orbit perigee by a variable amount. The electric propulsion system is then used to reach a circular medium Earth orbit (MEO) at 18,000 km altitude (24,378 km radius) and an inclination of 27° . No plane change is performed by the on-board chemical and electric systems. We would like to know the spacecraft mass at the mission orbit as a function of the park apogee and perigee altitudes. Specific impulse for the chemical system is 326 s, as expected from the technology trend for storable bipropellant engines. Current performance for $\text{N}_2\text{H}_4/\text{N}_2\text{O}_4$ liquid apogee engines is 322-324 s. For the electric system a specific impulse of 1600 s and a thrust-to-power ratio of

0.057 N/kW are assumed, as applies to a xenon Hall-effect thruster in this power range. The spacecraft has 9.2 kW of power available for propulsion at beginning of life and generates 0.524 N of thrust.

The launch vehicle is assumed to have the performance given in Figure 15, which shows the spacecraft mass in the elliptical park orbit as a function of apogee radius, with curves corresponding to seven different values of the perigee radius. Low-thrust acceleration is calculated from this initial mass. For example, if the initial mass is 4000 kg, the acceleration is $1.31 \times 10^{-7} \text{ km/s}^2$. The length of the apogee-centered burn arc and the out-of-plane thrust angle are chosen to minimize the product $\Delta V \times \Delta t$, which yields a favorable trade-off between propellant mass and trip time. In the present case, a plane change is not performed, and the out-of-plane thrust angle is zero. The first segment of the transfer uses case (1) steering where the acceleration vector is perpendicular to the orbit radius. This proceeds until the semimajor axis reaches its target value, at which time the steering program changes to case (3) with the acceleration vector perpendicular to the major axis of the ellipse. The orbit is thereby circularized at a constant semimajor axis using continuous thrusting.

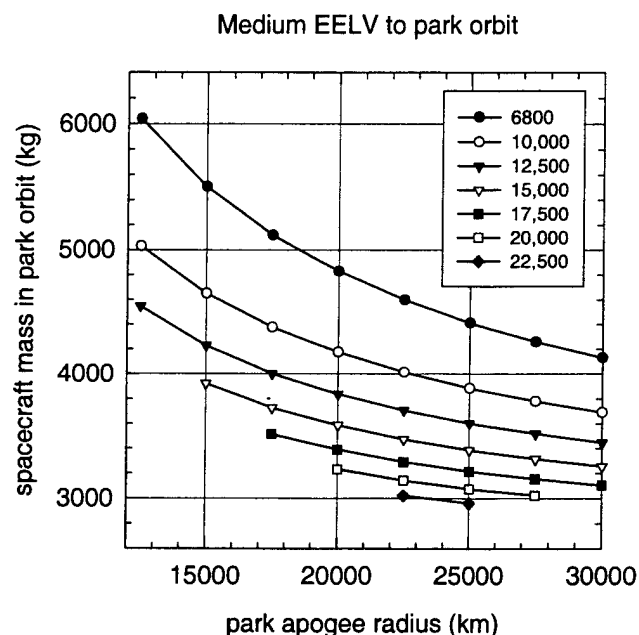


Figure 15. Spacecraft mass delivered by a medium launch vehicle to an elliptical park orbit at 27° inclination. Apogee radius is the independent variable, and the seven curves correspond to different perigee radii. The satellite is dropped off at an initial perigee altitude of 167 km, and the on-board chemical system (326 s specific impulse) raises the perigee radius to the values indicated.

Figure 16 shows the spacecraft mass at the final circular orbit as a function of trip time, with curves corresponding to six different values of the park apogee radius. The endpoints of these curves are connected by a curve representing the limiting case of a circle-to-circle spiral transfer with continuous thrusting. The mass benefit from the electric orbit transfer is given by the initial slope of the spiral transfer curve, amounting to 3.8 kg/day. A dry mass penalty of 40-80 kg would be imposed if the electric thrusters perform no function other than the initial orbit transfer. This is typically not the case,

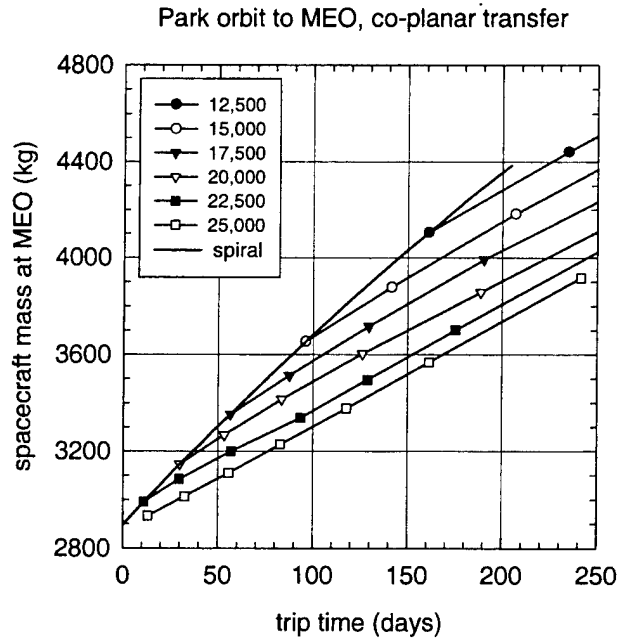


Figure 16. Spacecraft mass delivered to a circular MEO altitude of 18,000 km at 27° inclination, plotted as a function of trip time. The six curves with symbols correspond to different values of the apogee.

because the electric thrusters would also be used for stationkeeping and orbit disposal, and the dry mass penalty is assessed over the entire mission. A spiral transfer gives the maximum mass at MEO for a given trip time, assuming that no inclination change is needed. Hence, the best performance is obtained when the on-board chemical system circularizes the park orbit at the initial apogee altitude, and the electric thrusters operate continuously to raise the altitude to 18,000 km (24,378 km radius). Generally, an elliptical transfer will give better performance than a spiral transfer when a plane change is required from the on-board chemical and electric propulsion systems. This is the case in most geosynchronous transfers and in MEO transfers where the final inclination is different than that of the drop-off orbit.

Atmospheric Drag

Changes in the orbital elements produced by atmospheric drag can be calculated if the drag deceleration is known as a function of altitude. A detailed prediction of atmospheric density vs. altitude and epoch is beyond the scope of this study, and therefore a simplified approach was adopted. To demonstrate the orbit transfer analysis in typical missions at solar maximum conditions, drag deceleration f_{drag} was calculated for a three-axis stabilized satellite using the LIFETIME software developed by George Chao of The Aerospace Corporation's Astrodynamics Department.^{13,14} Results are shown in Figure 17 for nine altitudes between 180 km and 700 km at $i = 33^\circ$ along with polynomial least-squares fit of $\log f_{\text{drag}}$ vs. altitude. A linear extrapolation of this curve is used for altitudes greater than 700 km. Drag deceleration at any point in an arbitrary elliptical orbit can be calculated from Figure 17 using as input the altitude given by

$$h = a(1 - e \cos E) - r_{earth} . \quad (16)$$

The solar maximum data in Figure 17 are used for all of the examples that follow, but for a real mission the drag deceleration would need to be calculated using the appropriate epoch, inclination, and area-to-mass ratio. The drag deceleration vector is tangent to the orbit path, and therefore corresponds to the case (2) in-plane steering program. Secular rates of change of the semimajor axis and eccentricity are

$$\frac{da}{dt} = \frac{2}{\pi} \sqrt{\frac{a^3}{\mu}} \int_0^\pi f_{drag} \sqrt{1 - e^2 \cos^2 E} dE , \quad (17)$$

$$\frac{de}{dt} = \frac{2}{\pi} \sqrt{\frac{a}{\mu}} (1 - e^2) \int_0^\pi \frac{f_{drag} \cos E (1 - e \cos E)}{\sqrt{1 - e^2 \cos^2 E}} dE , \quad (18)$$

where f_{drag} is a function of a , e , and E . Drag-induced rates of change of a and e in Eqs. (17) and (18) are added to the thrust-induced rates of change to generate numerical results. In this treatment, i , Ω , and ω are unaffected by drag.

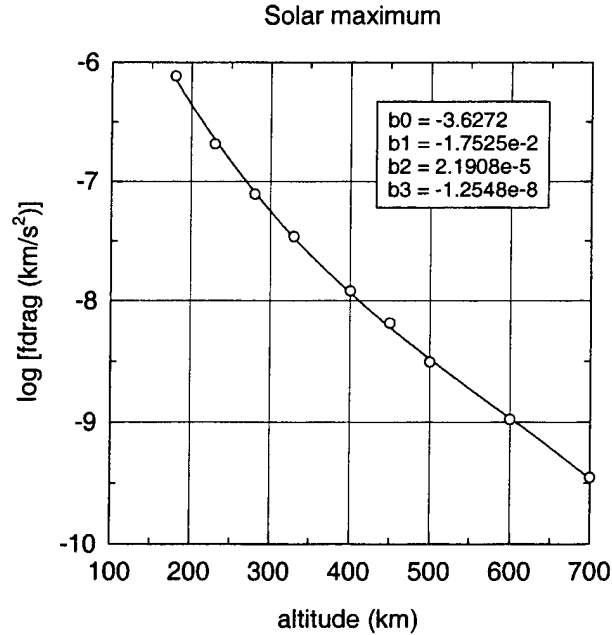


Figure 17. Logarithm of atmospheric drag deceleration for circular orbits with $i = 33^\circ$ for a 130-kg spacecraft. The solar array is sun-pointing with an area of 2.9 m^2 , and the 1.0-m^3 spacecraft body is nadir-pointing. The atmospheric density model is MSIS90 at solar-maximum conditions.^{13,14}

LEO Insertion

A key parameter in optimizing the deployment of low Earth orbit (LEO) constellations is the altitude at which satellites are dropped off by the launch vehicle. Lower drop-off altitude means a greater launch vehicle throw weight along with a higher ΔV to reach the mission orbit. If the spacecraft uses an electric propulsion system, then lowering the drop-off altitude causes ΔV to increase because of the additional time spent fighting atmospheric drag (this is in addition to the extra ΔV due only to the altitude change). Figures 18 and 19 show the low-thrust ΔV and trip time to reach a mission orbit at 800-km altitude as a function of the drop-off altitude and the spacecraft acceleration. Continuous thrusting is assumed, and the initial and final eccentricities are 0.0020 and 0.0001. The spacecraft cannot perform the climb-out if the drag force exceeds the thrust, and this is exemplified by the upturn in the ΔV and trip time curves as the drop-off altitude decreases. For initial altitudes greater than 400 km the drag force is small, and ΔV is nearly independent of thrust acceleration, namely

$$\Delta V = f \Delta t \approx \sqrt{\frac{\mu}{a^3}} \frac{\Delta a}{2}. \quad (19)$$

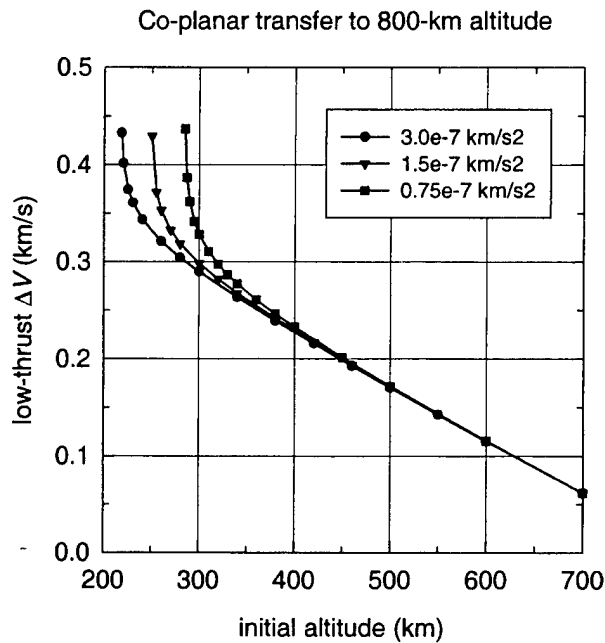


Figure 18. Velocity increment vs. initial mean altitude for co-planar transfer to an 800-km circular orbit with three values for the spacecraft acceleration.

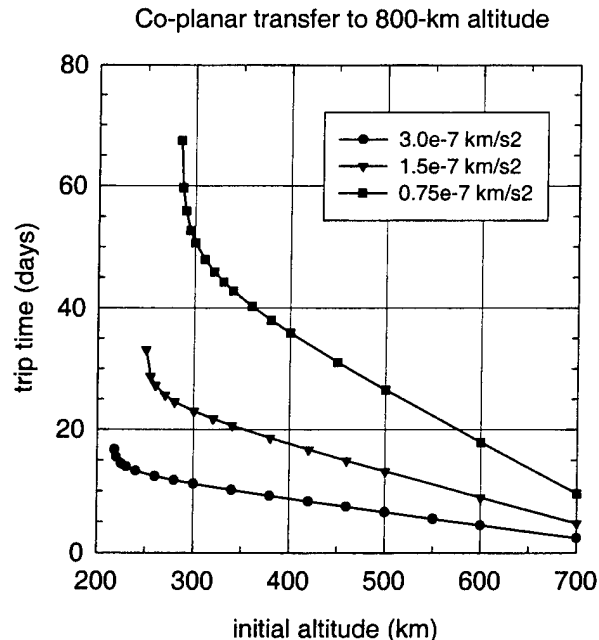


Figure 19. Trip time vs. initial mean altitude for co-planar transfer to an 800-km circular orbit with three values for the spacecraft acceleration.

Orbit Disposal

Large numbers of satellites are being launched into low Earth orbit (LEO) for applications such as personal communications, messaging, multimedia, and remote sensing. This could lead to a serious problem from orbital debris unless the satellites are removed from the mission orbit at the end of life. At GEO this task is accomplished by transferring to a 200-300 km higher altitude “graveyard” orbit, with a ΔV of 3.6 m/s per 100 km of altitude increase (this value applies to impulsive and low-thrust maneuvers). End-of-life disposal from LEO can be a demanding task in terms of ΔV for which high specific impulse thrusters are well suited. One method of disposal is by thrusting to lower the perigee of an initially circular orbit to the point where atmospheric drag will quickly lower the apogee until re-entry occurs. Alternatively, the spacecraft can be moved to the graveyard altitudes of 2000-2500 km, which have few other uses because of the severity of the natural radiation environment. For re-entry, we assume that mission ends when the semimajor axis reaches 6628 km, i.e., 250-km mean altitude. Apogee-centered burns are performed with a burn-arc angle of $\alpha = 105^\circ$, which is a reasonable compromise between saving propellant mass and reducing the trip time. Figure 20 shows a typical de-orbit altitude profile in which the eccentricity initially increases due to perigee-lowering and then decreases as drag lowers the apogee. Figure 21 shows the re-entry and graveyarding ΔV as a function of trip time for initial altitudes of 400-1600 km. For a given initial altitude the re-entry ΔV decreases slightly as the spacecraft acceleration is decreased, because there is a greater length of time for drag to contribute to the maneuver. Assuming that trip time is not a significant issue for orbit disposal, the choice of re-entry vs. graveyarding can be decided on the basis of ΔV . Propellant mass is minimized by choosing re-entry

when the initial altitude is less than 1200 km and graveyarding when the initial altitude is greater than 1300 km.

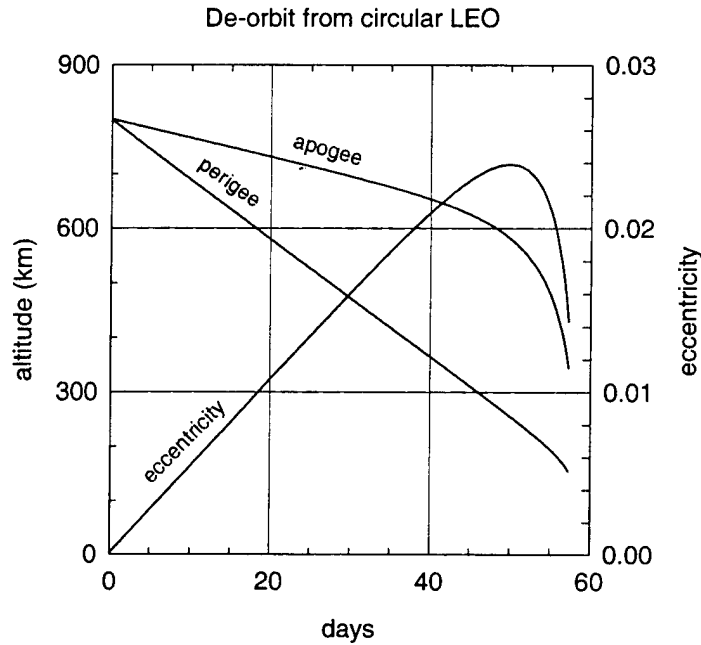


Figure 20. De-orbiting from an 800-km circular orbit via apogee-centered burn arcs with $f = 0.75 \times 10^{-7}$ km/s². The velocity increment is 218 m/s, and 57 days are required to reach a mean altitude of 250 km.

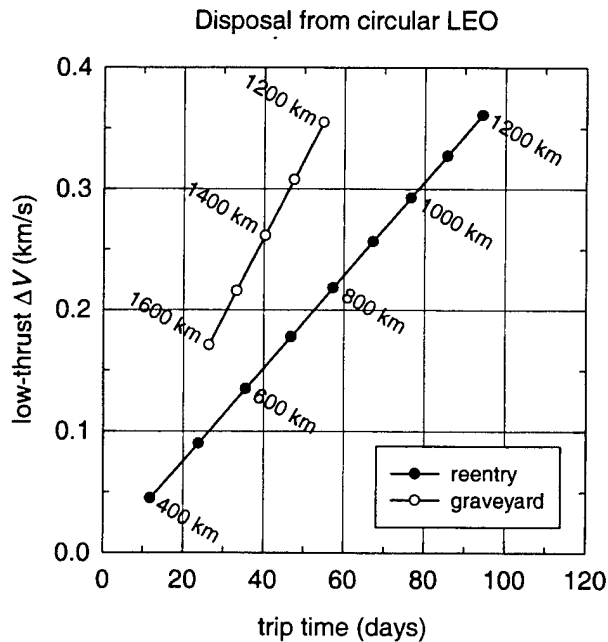


Figure 21. Velocity increment vs. trip time for disposal from near-circular orbits with initial altitudes of 400-1600 km. The spacecraft acceleration is $f = 0.75 \times 10^{-7}$ km/s². The graveyard orbit has a circular altitude of 2000 km.

Drag Compensation for Co-Orbiting Satellites

Controlling the in-track separation between co-orbiting satellites in LEO is required for missions such as stereo Earth-observation and formation flying. Rather than use thrusting to fully compensate the drag-induced altitude decay, it is usually sufficient to counteract the differential drag force between satellites having unequal area-to-mass ratios. We wish to evaluate the ΔV and thrusting time for differential drag compensation and for maneuvers to adjust the in-track separation. If the orbits are near-circular and gravitational perturbations are neglected, then the mean motion n and its secular rate of change dn/dt are given by

$$n = \frac{dM}{dt} = \frac{2\pi}{\tau} = \sqrt{\frac{\mu}{a^3}}, \quad (20)$$

$$\frac{dn}{dt} = -\frac{3}{2} \frac{n}{a} \frac{da}{dt} = -\frac{3f}{a}, \quad (21)$$

where M is the mean anomaly, and f is the vector sum of thrust plus drag acceleration. The thrust vector is assumed to be tangent to the orbit path. Integrating Eq. (21) yields the mean motion in the presence of constant thrusting,

$$\frac{dM}{dt} = \sqrt{\frac{\mu}{a^3}} = \sqrt{\frac{\mu}{a_0^3}} - \frac{3f}{a_0} (t - t_0), \quad (22)$$

where a_0 is the orbit radius at the starting time t_0 . In terms of the mean anomaly difference ΔM , the rate of change of the in-track separation between two satellites in a common orbit plane is

$$\frac{d\Delta M}{dt} = \sqrt{\frac{\mu}{a_2^3}} - \sqrt{\frac{\mu}{a_1^3}}, \quad (23)$$

$$\frac{d\Delta M}{dt} = \sqrt{\frac{\mu}{a_{2_0}^3}} - \sqrt{\frac{\mu}{a_{1_0}^3}} - 3(t - t_0) \left(\frac{f_2}{a_{2_0}} - \frac{f_1}{a_{1_0}} \right), \quad (24)$$

where a_{1_0} and a_{2_0} are the orbit radii of satellites 1 and 2 at the starting time t_0 . Here f_1 and f_2 are each the vector sum of thrust acceleration plus drag deceleration as given in Figure 17. For the special case of continuous thrusting where the initial orbit radii are equal, Eq. (24) is equivalent to the rate of phase shifting given in Edelbaum's Eq. (34).¹ In this case, integrating Eq. (24) yields a simple expression for the mean anomaly difference as a function of time,

$$\Delta M = \Delta M_0 - \frac{3(f_2 - f_1)}{2a_0} (t^2 - t_0^2). \quad (25)$$

Numerical results are obtained by integrating Eq. (23) simultaneously with equations for the rates of change of the satellite altitudes and the rate of ΔV build-up. The examples in Figs. 22 and 23 are for near-circular orbits where satellite 1 is assumed to be passive, and satellite 2 has a maneuvering capability. Satellite 2 has an area-to-mass ratio that is 10% greater than that of satellite 1, and hence its

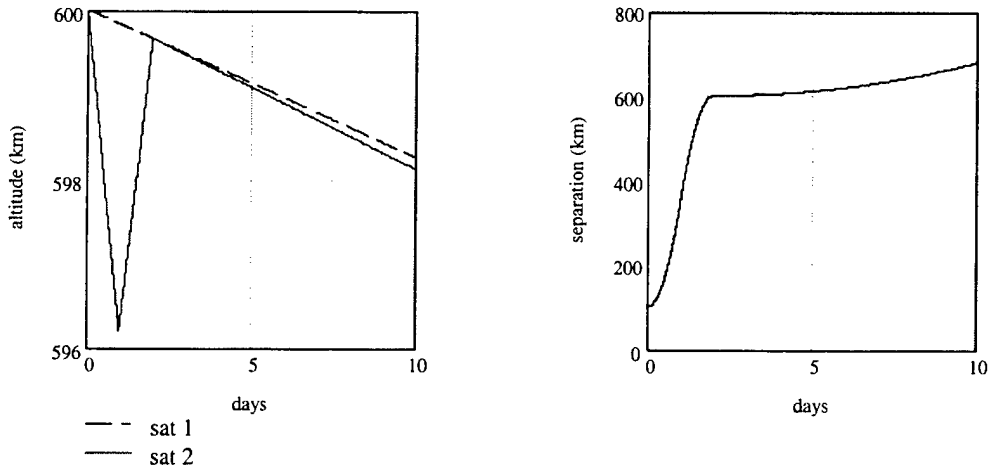


Figure 22. Changing the in-track separation between two co-orbiting satellites in the presence of atmospheric drag. Thrust acceleration of satellite 2 is $0.75 \times 10^{-7} \text{ km/s}^2$ during two symmetrical 15-minute burns per revolution. The ΔV for this maneuver is 3.94 m/s and the trip time is 1.96 days.

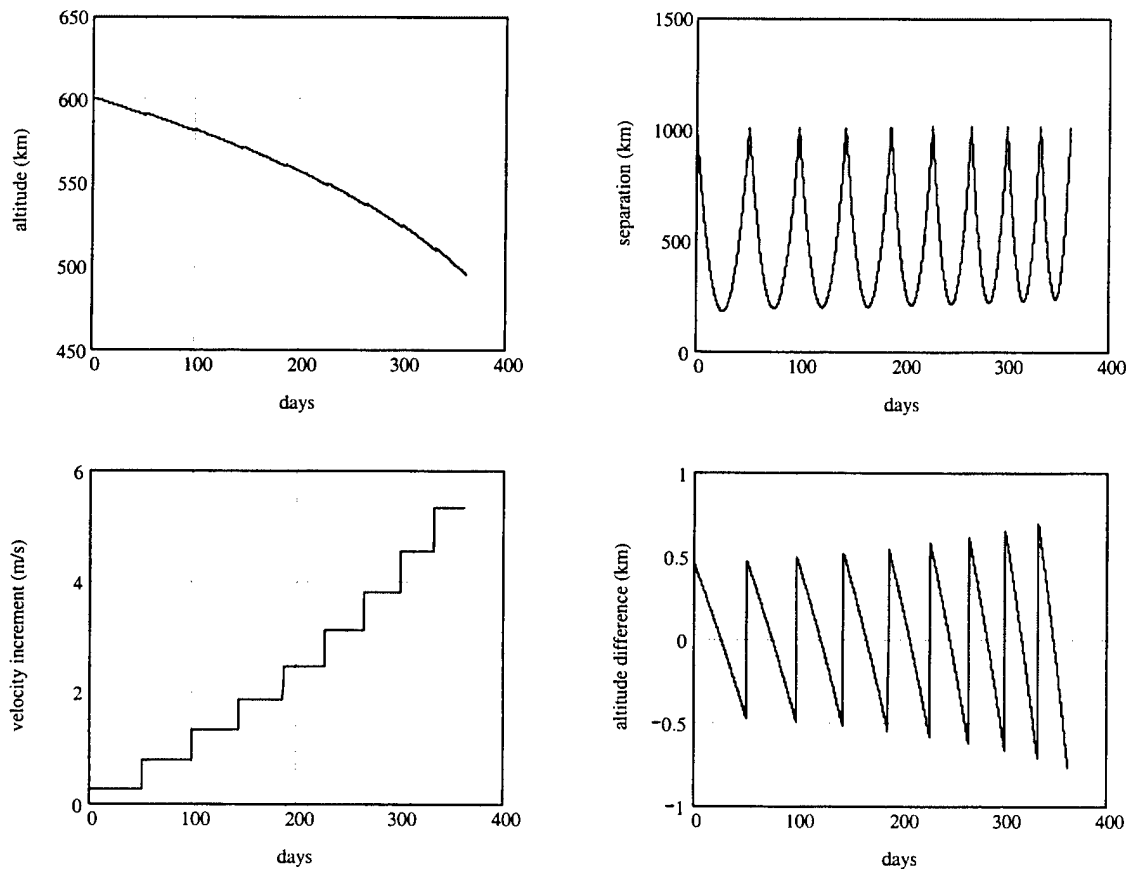


Figure 23. Controlling the separation distance between two co-orbiting satellites over a 1-year mission. Satellite 1 is passive, while satellite 2 (which has a 10% greater area-to-mass ratio) uses periodic thrusting to raise its altitude above that of satellite 1. The ΔV for the 1-year mission is 5.3 m/s.

altitude decays more rapidly. Figure 22 shows a maneuver to increase the in-track separation from 100 km to 600 km in 2.0 days beginning at an altitude of 600 km. Tangential thrusting by satellite 2 decreases the altitude until half the desired phase shift is accumulated. Reversing the thrust direction returns satellite 2 to the altitude of satellite 1. Maneuvers are performed with two symmetrical burns per revolution to maintain a near-circular orbit. Each burn is nominally 15 minutes duration, but the outbound leg and the inbound leg have burn times that differ slightly ($< 2\%$) to compensate for differential drag during the maneuver. When the thrust vector points in the (+) in-track direction for altitude raising, a greater than nominal impulse is required because the drag deceleration vector is in the (−) in-track direction. Conversely, for altitude lowering a less than nominal impulse is needed. There is no compensation following the maneuver, so that the in-track separation continues to increase slowly after the target value of 600 km is reached.

Figure 23 is an example of differential drag compensation between two satellites over a 1-year mission starting at 600-km altitude and concluding at 497 km. Periodic maneuvers are performed by satellite 2 to match the average rate of altitude decay of satellite 1. At the start of a cycle, satellite 2 is 1000 km ahead of satellite 1 and 0.4-0.7 km lower in altitude. Two 15-minute burns per orbit with $f = 0.75 \times 10^{-7} \text{ km/s}^2$ are repeated over 4-6 revolutions to raise the relative altitude by 0.8-1.4 km, from which point satellite 2 decays back to its initial relative altitude. Separation distance decreases in the first half of the drift period, returning to the initial 1000-km separation at the end, with closest approach occurring when the satellites are at the same altitude. The cycle time decreases from 51 days initially to 29 days on the last cycle, because the increase in drag force requires more frequent corrections. In this example the separation distance varies by $\pm 397 \text{ km}$ averaged over the mission. For a tighter tolerance the maneuvers must be performed more often, but the build-up rate of ΔV is independent of separation tolerance. Figure 24 shows the dependence of cycle time on altitude and separation tolerance. For example, to achieve a tolerance of $\pm 100 \text{ km}$ the cycle time is 7 days at 400-km altitude and 45 days at 700-km altitude.

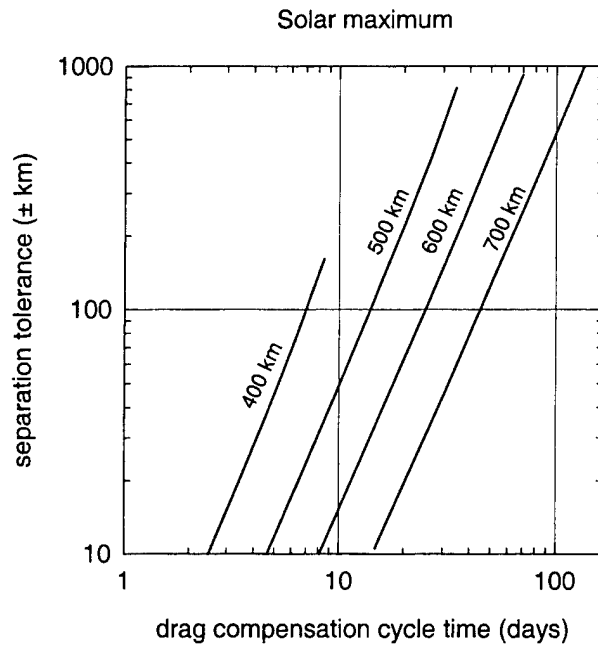


Figure 24. Separation tolerance vs. cycle time for differential drag compensation by two co-orbiting satellites having area-to-mass ratios that differ by 10%. Results are displayed at four circular altitudes with solar maximum conditions.

References

- ¹T.N. Edelbaum, "Propulsion requirements for controllable satellites," *ARS Journal*, 31, 1079 (1961).
- ²References are listed in J.E. Pollard and S.W. Janson, "Spacecraft electric propulsion applications," ATR-96(8201)-1, The Aerospace Corporation (1 Feb 1996), sec. 5, p. 34.
- ³F. Porte, et al. "Application of ion propulsion system to communications spacecraft," Paper IEPC-93-015, 23rd International Electric Propulsion Conference, 13-16 Sept 1993, Seattle, WA.
- ⁴S.R. Oleson and R.M. Myers, "Launch vehicle and power level impacts on electric GEO insertion," Paper AIAA-96-2978, 32nd Joint Propulsion Conference, 1-3 July 1996, Lake Buena Vista, FL.
- ⁵A.G. Schwer and E. Messerschmid, "System and mission optimization of geostationary telecommunication satellites using arcjet propulsion systems," Paper AIAA-97-2713, 33rd Joint Propulsion Conference, 6-9 July 1997, Seattle, WA.
- ⁶C.A. Kluever and S.R. Oleson, "Direct approach for computing near-optimal low-thrust Earth-orbit transfer missions," *J. Spacecraft and Rockets*, 35, 509-515 (1998).
- ⁷J.A. Kechichian, "Orbit raising with low-thrust tangential acceleration in presence of Earth shadow," *J. Spacecraft and Rockets*, 35, 516-525 (1998).
- ⁸J.A. Kechichian, "Low-thrust inclination control in presence of Earth shadow," *J. Spacecraft and Rockets*, 35, 526-532 (1998).
- ⁹C.R. Koppel, "Advantages of a continuous thrust strategy from a geosynchronous transfer orbit, using high specific impulse thrusters," 14th International Symposium of Space Flight Dynamics, ISSFD-XIV, 8-12 Feb 1999, Foz de Iguaçu, Brasil.
- ¹⁰E.G.C. Burt, "On space manoeuvres with continuous thrust," *Planet. Space Sci.* 15, 103-122 (1967).
- ¹¹A. Spitzer, "Near optimal transfer orbit trajectory using electric propulsion," Paper AAS-95-215, Spaceflight Mechanics Meeting, 13-16 Feb 1995, Albuquerque, NM.
- ¹²Chao, C.C., "Introduction to orbit perturbation," *Orbital Mechanics*, V.A. Chobotov, ed. AIAA, Washington, DC, ch. 8, p. 210 (1991).
- ¹³C.C. Chao, "Program LIFETIME User's Guide," Aerospace Report No. ATR-95(5917)-1, September 1995.
- ¹⁴A.E. Hedin, "Extension of the MSIS thermosphere model into the middle and lower atmosphere," *Journal of Geophysical Research*, Vol. 96, No. A2, February 1991, pp. 1159-1172.

Appendix 1

From Reference 12, the mean mean-motion \bar{n} and the natural drift rates of Ω and ω (i.e., nodal regression and apsidal rotation) are

$$\bar{n} = \sqrt{\frac{\mu}{a^3}} \left[1 + \frac{3}{2} J_2 \frac{r_e^2}{p^2} \left(1 - \frac{3}{2} \sin^2 i \right) \sqrt{1 - e^2} \right], \quad (\text{A1})$$

$$N \equiv \frac{d\Omega}{dt} = -\frac{3}{2} J_2 \frac{r_e^2}{p^2} \bar{n} \cos i, \quad (\text{A2})$$

$$A \equiv \frac{d\omega}{dt} = \frac{3}{4} J_2 \frac{r_e^2}{p^2} \bar{n} (4 - 5 \sin^2 i), \quad (\text{A3})$$

where $p = a(1 - e^2)$, Earth's equatorial radius is $r_e = 6378.137$ km, the second zonal harmonic of the geopotential is $J_2 = 0.00108263$, and the orbit period is $\tau = 2\pi/\bar{n}$. In this report, the analytical results for secular rates of change of the elements under various steering programs assume that the period is $\tau \approx 2\pi\sqrt{a^3/\mu}$. This approximation enables the derivation of closed-form solutions for the velocity increment and trip time. For numerical solutions the secular rates can be modified to incorporate the J_2 effect on τ , although the magnitude of this effect is quite small.